Absorption spectroscopy on room temperature excitonic transitions in strained layer InGaAs/InGaAlAs multiquantum-well structures

Y. Hirayama,[a] Woo-Young Choi, L. H. Peng,[b] and C. G. Fonstad
Department of Electrical Engineering and Computer Science and Research Laboratory of Electronics, Massachusetts Institute of Technology, Cambridge, Massachusetts 02139

(Received 14 December 1992; accepted for publication 1 March 1993)

The physical properties (transition energy, oscillator strength, linewidth, binding energy, and reduced effective mass) of room temperature excitons in compressively strained InGaAs/InGaAlAs multiquantum-well (MQW) structures as a function of the well width have been investigated for the first time by both absorption measurements and photomodulated transmittance measurements. Photomodulated transmittance spectroscopy has been successfully applied to clearly reveal critical transition points. Measured transition energies are in good agreement with a model which includes the heavy hole and light hole splitting due to the strain. For well widths of 2.5–7.5 nm, oscillator strengths are smaller for the strained layer MQWs than for the lattice-matched MQWs by 35%–45%. This is due to the larger exciton radius for the strained MQWs resulting from smaller in-plane reduced effective masses (0.031–$0.038m_0$), which are 65% of those of the lattice-matched MQWs.

I. INTRODUCTION

An exciton, which is in fact a many body effect, consists of an electron and a hole interacting with each other through Coulomb attraction. It is well known in quantum wells that exciton effects are enhanced because of the wave function confinement perpendicular to the quantum well plane. Strong exciton resonances in quantum wells have been reported.[1–14] Among many multiquantum-well (MQW) structures, strained layer MQW structures[16–18] have been intensively studied in recent years for their application to high performance optical devices such as low threshold, high-power, and high-speed lasers.[19–34] Especially, the strained layer InGaAs/InAlAs, InGaAs/InGaAlAs, and InGaAs/InP material systems are attractive and important, because these materials emit or absorb the light at around 1.55 μm wavelength, which is the optimal wavelength for optical communication systems. Therefore, a systematic understanding of the behavior of excitons in strained layer MQWs in these material systems is very important for advanced photonic devices. Only few results on the basic optical properties have been reported,[13–15] however, and the important physical parameters of the excitons in the strained layer MQWs as a function of the well width have not yet been determined.

In this paper, the physical properties of excitons, i.e., transition energy, oscillator strength, linewidth, binding energy, and reduced effective mass, in strained layer MQWs based on long-wavelength materials are presented. To the authors' knowledge, this is the first systematic report on the room temperature excitons in long-wavelength strained layer MQWs. Photomodulated transmittance spectroscopy is found to be a more effective way to reveal the subband structures compared with conventional absorption measurement. Important results which show weaker excitonic transitions for the compressively strained MQWs resulting from smaller reduced effective masses are described.

II. EXPERIMENTS

A. Sample structures

Three kinds of strained layer InGaAs/InGaAlAs MQW structures with different well thicknesses (samples A, B, and C) were grown on (001) InP:Fe substrates by molecular beam epitaxy (MBE). For comparison, a lattice matched InGaAs/InAlAs structure (sample D) was also fabricated. The well thickness in each sample was precisely determined by fitting a simulated satellite pattern to x-ray diffraction spectra.[35] Table I summarizes the sample structures. Samples A, B, and C contain four 2.5 nm wells, four 5.0 nm wells, and four 7.5 nm wells, respectively. The Indium composition in the InGaAs ternary compound is determined to be 0.652 for sample C and almost same for samples A and B. This corresponds to 0.83% compressive strain in the plane of the quantum well. The wells in each sample are separated by 8.5 nm thick $In_{0.470}Ga_{0.255}Al_{0.275}As$ barriers which have 0.43% tensile strain. Although the total well thickness for sample C is more than a critical thickness,[36] the strain is not relaxed, partly because the growth temperature is lowered[37] and partly because the total strain is compensated by the tensile strained barriers. The upper and lower cladding layers have the same composition as the barriers and are 0.12 and 0.16 μm thick, respectively. They are doped with Si and Be for n and p type, respectively, to 5×10^{17} cm^{-3} except 0.04 μm undoped regions in each layer which cover the MQW region. These thin undoped layers are employed to avoid any dopant diffusion into the MQW region, which is unintentionally doped. This p-i-n structure is helpful for the photomodulated transmittance measurements as will be described later. The reference sample D consists of 40

[a]On leave from Toshiba Co., Research and Development Center, Kawasaki, Japan.
[b]Division of Applied Sciences, Harvard University, Cambridge, MA 02138.

 0021-8979/93/74(1)/570/9/$6.00

TABLE I. Structural parameters of the samples investigated. L_z and L_b are the well width and barrier width, respectively. Samples A–C have compressively strained InGaAs quantum wells with InGaAlAs barriers. Sample D has lattice-matched InGaAs quantum wells with InAlAs barriers.

Sample	No. of well	L_z (nm)	L_b (nm)	In composition
	4			
	4			
	4			
	40			

lattice-matched quantum wells with 7.2 nm thickness and InAlAs barriers with 7.2 nm thickness. The whole structure is unintentionally doped for this sample. Details of the sample growth have been reported elsewhere.[35]

B. Absorption measurements

We measured the optical absorption spectra of the samples at room temperature by conventional phase-sensitive lock-in technique using a monochromator and a tungsten (W) lamp. A PbS detector was used for light detection. For these measurements, the rear side of the samples were polished by Br-methanol to avoid light scattering. A perpendicular incidence geometry was employed. The absorption coefficient was determined by comparing the transmitted light intensity with (I_1) and without (I_2) the sample. By definition of the transmission coefficient T, we obtain the following relation between these two quantities:

$$T=I_1/I_2=(1-R)^2\exp(-\alpha d)/[1-R^2\exp(-2\alpha d)], \quad (1)$$

where R is reflection coefficient, α is absorption coefficient, and d is total thickness of well layer. The absorption coefficient which is measured from a transparent point below the bandgap energy takes the following form:

$$\alpha_{\mathrm{MQW}}=\alpha-\alpha'=\ln(T'/T)/d[1+x(\alpha)], \quad (2)$$

where α' is the absorption value at almost transparent point. The calibration factor $x(\alpha)$ is expressed as

$$x(\alpha)=\ln\{[1-R^2\exp(-2\alpha d)]/[1-R^2\exp(-2\alpha' d)]\}/(\alpha-\alpha')d, \quad (3)$$

and the value is found to be around 0.2 for our structures. For samples A and B, more than one piece of wafer are stacked and measured to improve the signal-to-noise ratio.

C. Photomodulated transmittance measurements

Modulation optical spectroscopy is a very attractive technique because of its high sensitivity. The photomodulated transmittance (PMT) technique[38,39] is similar to photoreflectance (PR) spectroscopy.[40–42] For structures grown on transparent substrates, sample thinning is not necessary, which makes the transmittance measurement technique more attractive. Moreover, spectra can become less complicated because the substrate contribution is almost completely suppressed. The photomodulated transmittance is produced by a contactless electric field modulation by means of a laser beam. Ar laser light at 1 mW power was chopped and shone on the sample as shown in Fig. 1. A strong increase in both resolution and signal-to-noise ratio compared with the conventional room temperature transmission spectroscopy was obtained by the addition of a modulated light source. It is found that this technique is much more sensitive when it is used for the *p-i-n* structure which has a relatively strong built-in electric field.

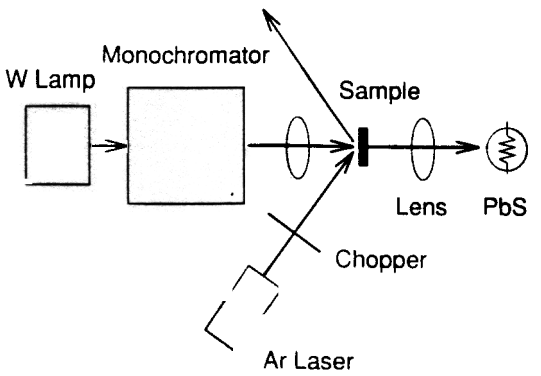

FIG. 1. The photomodulated transmittance measurement setup. Chopped Ar laser light at a power of 1 mW was used to modulated the internal built-in field in a sample.

III. RESULTS AND DISCUSSION

A. Transition energy

Figure 2 shows the measured room temperature absorption spectra for three kinds of the strained layer MQWs (samples A, B, and C) and the lattice matched MQW (sample D). The arrows indicate calculated excitonic transition energies. Clear transitions between e1 (first subband in a conduction band) and hh1 (first subband in a heavy hole valence band) are observed for all samples. The energy values are 0.897 (and also 0.913), 0.792, 0.731, and 0.835 eV for samples A–D, respectively. However, critical points are not always clear for higher order transitions.

Figure 3 shows the corresponding photomodulated spectra. As shown in Fig. 3, PMT signals are very sensitive at critical points. In these figures, the conventional absorption spectrum is superimposed for comparison. The arrows indicate calculated excitonic transition energies. The PMT signals are stronger by an order of magnitude for samples A, B, and C, which have the *p-i-n* structure, compared with those for sample D, which is unintentionally doped. The signal level is of the order of 10^{-3}. This is thought to be due to the relatively strong built-in electric field in the strained layer MQW samples.

In general, the absorption change, $\Delta\alpha$, in the PMT measurement is proportional to the change in the imaginary part of the dielectric function, $\Delta\epsilon_i$ resulting from the change in the intensity of the pump beam P. For excitonic transitions, $\Delta\epsilon_i$ can be expressed as[41,42]

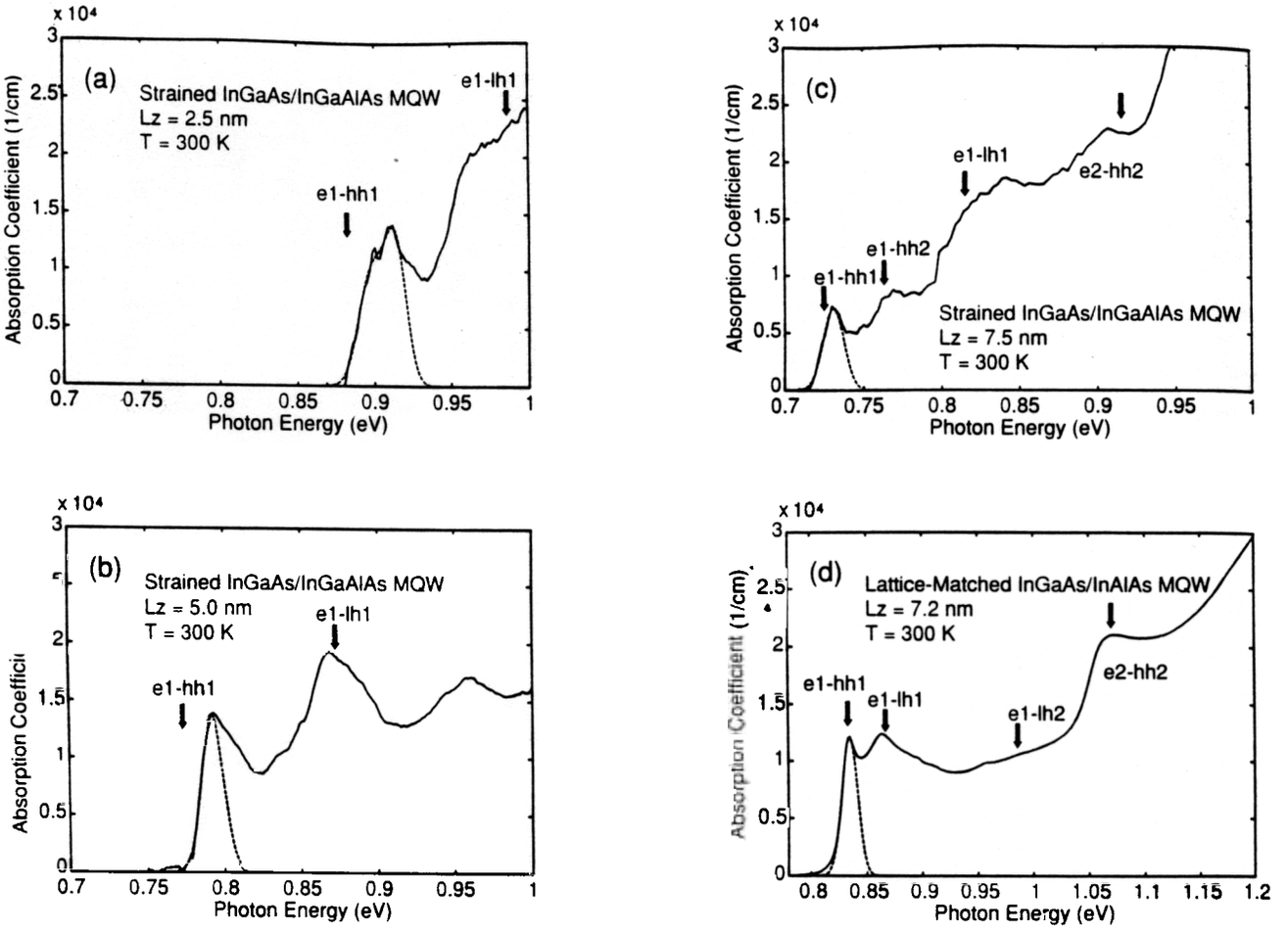

FIG. 2. Room temperature absorption spectra (solid line) and fitted Gaussian curves (dashed line). (a) Sample A has strained layer MQW with 2.5 nm well width. The arrows indicate calculated energies for $e1$-hh1 (0.882 eV) and $e1$-lh1 (0.985 eV) transitions. (b) Sample B has strained layer MQW with 5.0 nm well width. The arrows indicate calculated energies for $e1$-hh1 (0.772 eV) and $e1$-lh1 (0.872 eV) transitions. (c) Sample C has strained layer MQW with 7.5 nm well width. The arrows indicate calculated energies for $e1$-hh1 (0.726 eV), $e1$-hh2 (forbidden 0.761 eV), $e1$-lh1 (0.815 eV), and $e2$-hh2 (0.915 eV) transitions. (d) Sample D has lattice matched MQW with 7.2 nm well width. The arrows indicate calculated energies for $e1$-hh1 (0.833 eV), $e1$-lh1 (0.867 eV), $e1$-lh2 (forbidden 0.986 eV), and $e2$-hh2 (1.070 eV) transitions.

$$\Delta\epsilon_i=\left(\frac{\partial\epsilon_i}{\partial E_{\rm ph}}\right)\left(\frac{\partial E_{\rm ph}}{\partial P}\right)+\left(\frac{\partial\epsilon_i}{\partial\Gamma}\right)\left(\frac{\partial\Gamma}{\partial P}\right)+\left(\frac{\partial\epsilon_i}{\partial S}\right)\left(\frac{\partial S}{\partial P}\right), \quad (4)$$

where $E_{\rm ph}$ is the exciton energy gap, Γ is a phenomenological broadening parameter, and S is the integrated intensity of the excitonic transition. The relative contributions to the PMT line shape arising from the linewidth, energy gap, and intensity modulation mechanisms are determined by the magnitude of the bracketed coefficients in Eq. (4). These coefficients are functions of the pump intensity and the subband indices of the excitons. When the first term in Eq. (4) is dominant, the line shape will be a dispersive shape, which has both positive and negative parts, and the zero crossing point gives the excitonic transition energy. When the second or the third term is dominant, the line shape will be symmetric and the peak gives the excitonic transition energy. This relationship is schematically drawn in Fig. 4. In actual cases, it is thought that the signal shape is the combination of three limiting cases described above. Therefore, the interpretation of PMT signals is not always easy and it should be done carefully, but it gives not only complementary information but also useful clues to reveal critical points. Empirically, in many cases, a middle point between a peak and a bottom in the PMT signal peak corresponds to a critical point in the absorption spectra. They can be attributed to excitons composed of electrons and heavy holes, and electrons and light holes. The excitonic transition energies for $e1$-lh1 are determined to be 0.99, 0.87, 0.81, and 0.86 eV for samples A–D, respectively. For samples C and D, the excitonic transitions from hh2 to $e2$ are also observed. Parity forbidden transitions between $e1$ and hh2 and between $e1$ and lh2 are also revealed in samples C and D, respectively. Sample D shows extra peaks near the band edge which we cannot yet explain.

The excitonic transition energies were calculated by using effective-mass approximation including heavy hole and light hole energy split at the gamma point due to strain. The effect of strain on the band lineups was calculated in a straightforward manner based on the model solid theory proposed by Van de Walle and Martin.[43,44] The energy shifts of an averaged valence band position $E_{v,\rm av}$ and a conduction band position E_c induced by the hydrostatic strain component can be expressed as

$$dE_{v,\rm av}=a_v(\Delta\Omega/\Omega) \quad (5)$$

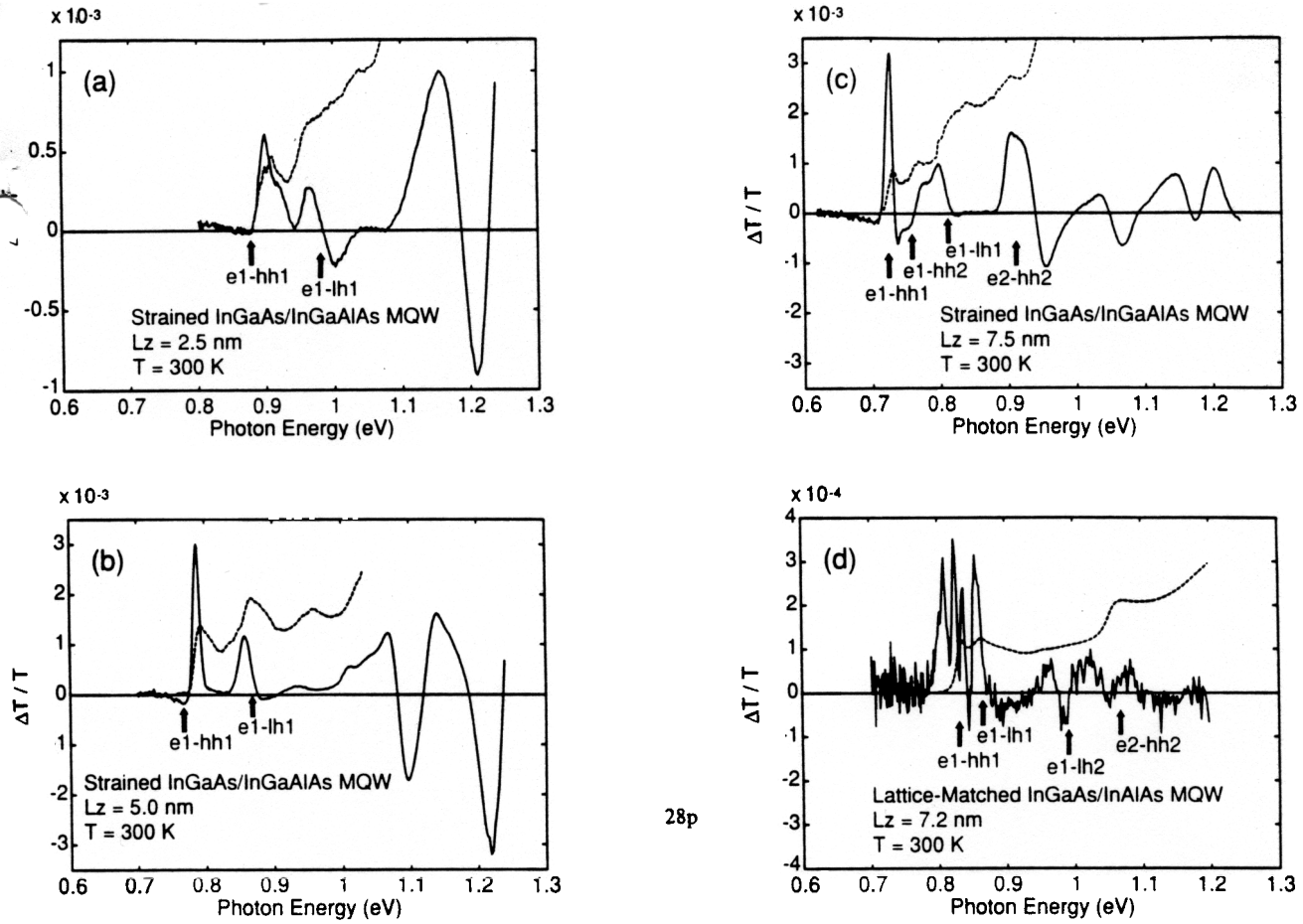

28p

FIG. 3. Room temperature photomodulated absorption spectra. Absorption spectra are superimposed for comparison. The arrows indicate calculated transition energies. (a) Sample A, (b) sample B, (c) sample C, (d) sample D.

$$dE_c = a_c(\Delta\Omega/\Omega), \tag{6}$$

where a_v and a_c are the hydrostatic deformation potentials for the valence and conduction bands, respectively. The $\Delta\Omega/\Omega$ is the fractional volume change which, for small strains on (001) substrates, can be approximated by

$$\Delta\Omega/\Omega = (2e_{xx} + e_{zz}), \tag{7}$$

where the strain components (e_{ij}) are defined as

$$e_{xx} = (a_0/a - 1), \tag{8}$$

$$e_{zz} = (-2c_{12}/c_{11})e_{xx}, \tag{9}$$

where a_0 is the lattice constant of InP, a is the lattice constant of the free-standing InGaAs epilayer, and C_{ij} is the elastic stiffness constant of InGaAs. The valence band degeneracy at the gamma point is lifted by the shear strain component. The energy shifts for the heavy hole ($|J,m_j\rangle = |3/2,3/2\rangle$) valence subband, the light hole ($|3/2,1/2\rangle$) subband, and the split-off band ($|1/2,1/2\rangle$) are calculated with respect to their weighted average and given by

$$dE_{v,\mathrm{hh}} = \Delta_0/3 - \delta E_{001}/2, \tag{10}$$

$$dE_{v,\mathrm{lh}} = -\Delta_0/6 + \delta E_{001}/4 + \mathrm{sp}, \tag{11}$$

$$dE_{v,\mathrm{so}} = -\Delta_0/6 + \delta E_{001}/4 - \mathrm{sp}, \tag{12}$$

with

$$\mathrm{sp} = 1/2[\Delta_0^2 + \Delta_0\delta E_{001} + 9/4(\delta E_{001})^2]^{1/2}, \tag{13}$$

where Δ_0 is the spin-orbit splitting in the unstrained bulk InGaAs, and δE_{001} is given by

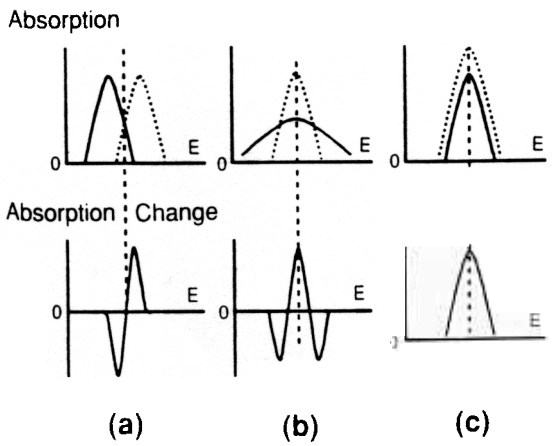

FIG. 4. Schematic photomodulated transmittance line shapes for three limiting cases: (a) dispersion like line shape due to transition energy change, (b) symmetric line shape due to linewidth change, (c) symmetric line shape due to transition intensity change.

TABLE II. Material parameters for the binary compound InAs, GaAs, and AlAs. Lattice constant, a_0; elastic modulus, C_{ij}; shear deformation potential, b; spin-orbit splitting, Δ_0; weighted average over the three uppermost valence bands at gamma, $E_{v,av}$; hydrostatic deformation potential for the valence band, a_v, and for the conduction band, a_c; and the electron, heavy hole, and light hole effective masses at gamma, m_e, m_{hh}, and m_{lh}, respectively. Interpolated values for ternary (InGaAs and InAlAs) and quaternary (InGaAlAs) materials are used for calculation.

		InAs[a]	GaAs[a]	AlAs[b]
a_0	Å	6.0584	5.6533	5.65
c_{11}	10^{11} dyn/cm^2	8.329	11.88	12.5
c_{12}	10^{11} dyn/cm^2	4.526	5.38	5.34
b	eV	−1.8	−1.7	−1.5
Δ_0	eV	0.38	0.34	0.28
$E_{v,av}$	eV	−6.67	−6.92	−7.49
a_v	eV	1.00	1.16	2.47
a_c	eV	−5.08	−7.17	−5.64
m_{hh}	m_0	0.41	0.45	0.409
m_{lh}	m_0	0.025	0.082	0.153
m_e	m_0	0.023	0.067	0.13

[a]Reference 15.
[b]Reference 43.

$$\delta E_{001}=2b(e_{zz}-e_{xx}), \tag{14}$$

where b is the shear deformation potential for a strain of tetragonal symmetry. The numerical parameters are calculated by Vegard's law from the binary compound data. The parameters for binary materials are listed in Table II.[15,43] Band gaps for $In_{1-x}Ga_xAs$ (this is obtained by an interpolation of the band gap for GaAs, InAs, and $In_{0.53}Ga_{0.47}As$) and $In_{1-x-y}Ga_yAl_xAs$[45] at room temperature are expressed as

$$E_g(\text{InGaAs})=0.36+0.6212x+0.4438x^2, \tag{15}$$

$$E_g(\text{InGaAlAs})=0.36+2.093x+0.629y+0.577x^2 +0.436y^2+1.013xy-2.0xy(1-x-y), \tag{16}$$

respectively. The InGaAs/InGaAlAs band lineups used for the calculation are shown in Fig. 5. The subband energies were calculated by an effective mass envelope function approach. Band nonparabolicity associated with the real wave vector in the conduction band of the well was taken into account as follows:[46]

$$m_e=m_{e0}(1+\alpha E), \tag{17}$$

$$\alpha=(1-m_{e0}/m_0)^2/E_g, \tag{18}$$

where m_e is electron mass at an energy E, m_{e0} is band bottom mass, and m_0 is free electron mass. For simplicity, valence band effective masses of the unstrained bulk materials were used, although the strain causes complicated valence band nonparabolicity. Continuity of the envelope function $\varphi(z)$ and of $[1/m(E)]d\varphi(z)/dz$ were used as boundary conditions. The absorption energy is given by

$$E_{ph}=E_e+E_h+E_g-E_b, \tag{19}$$

where E_e and E_h are electron and hole subband energies in the quantum well, E_g is the band gap of the well material,

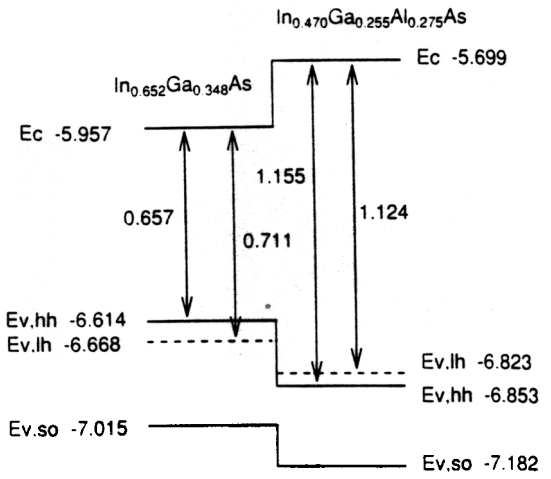

FIG. 5. The band lineups of strained InGaAs and InGaAlAs used for calculations.

and E_b is the exciton binding energy. The calculated transition energy and experimental results were plotted in Fig. 6. Although no fitting parameter is used, they are in good agreement, which confirms that the strain effect causes splitting of the heavy hole band and the light hole band. Uncertainty in material parameters such as effective mass, band discontinuity, and bandgap especially for InGaAlAs[47] is thought to be a cause of slight difference in experimental and calculated values. The relatively strong built-in field may also modify the transition energy, however, it is estimated to be less than several meV. The higher order transitions and the parity forbidden transitions observed in the PMT spectra also match the calculated transition energy very well.

B. Oscillator strength

It is well known that the excitonic transition is well fitted by a Gaussian distribution function.[1,12] By fitting the data using the Gaussian line shape, the integrated intensity S was obtained. Nonlinear least square method was used

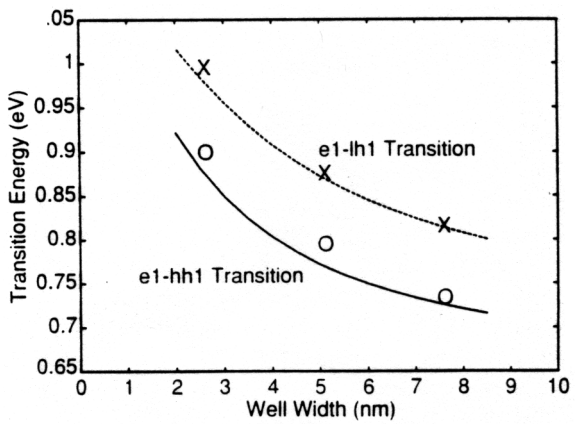

FIG. 6. Excitonic transition energies for $e1$-hh1 (circle) and $e1$-lh (cross) as a function of well width. Solid and dashed curves show calculated values for $e1$-hh1 and $e1$-lh1, respectively.

TABLE III. Fitted values of Gaussian fitting $\{a(E)=a_0\exp[-(E-E_{ph})^2/(2\Gamma^2)]\}$ for absorption spectra; a nonlinear least square method was used in the fitting. For Sample A, a mixture of two Gaussian curves was fit to the spectrum.

Sample	a_0 (cm^{-1})	E_{ph} (eV)	Γ (meV)
B			
C			
D			

for the data fitting. In Fig. 2, the fitted curves are plotted. For samples A–C, the built-in field may cause slight changes in the absorption spectra. However, the change in an absorption area is negligibly small according to the sum rule.[5] The integrated intensity is proportional to an oscillator strength divided by the well width L_z. For sample A, two mixed Gaussian shapes are used for the fitting because both the absorption spectrum and the PMT spectrum show double peaks at the absorption edge. The fitted values are listed in Table III. The absorption coefficients for $e1$-hh1 excitonic transition are 9550 (and also 12 320), 13 840, 7200, and 12 170 cm^{-1} for samples A–D, respectively. Figure 7 shows the integrated intensity as a function of the well width. The data for lattice-matched MQWs from Refs. 8 and 12 are also plotted. In Ref. 8, the data are taken at low temperature, however, it is reported that the temperature dependence of oscillator strength is very small.[12] It is found that S is smaller by 35%–45% for the strained layer MQWs than those for the lattice-matched MQWs at the same well width. At the same wavelength, however, S is almost same for both strain and lattice-matched MQW structures. It seems that the well width dependence of S is $1/L_z^2$ for both strained and lattice-matched MQWs when L_z is more than 5 nm,[48,49] while it is less dependent on the well width for narrower well widths.

It is very important to know the spatial extent of the exciton, λ_{ex}, in the quantum well because this information is useful in understanding the broadening of the exciton

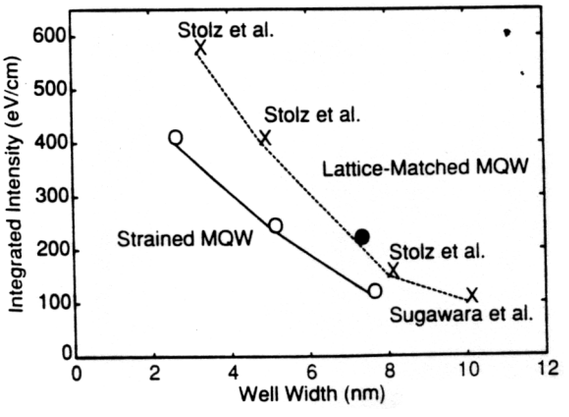

FIG. 7. Integrated intensity as a function of well width for strained (open circle) and lattice-matched (closed circle) quantum wells. The data from Refs. 8 and 12 are also included (cross). The lines are a guide to the eye.

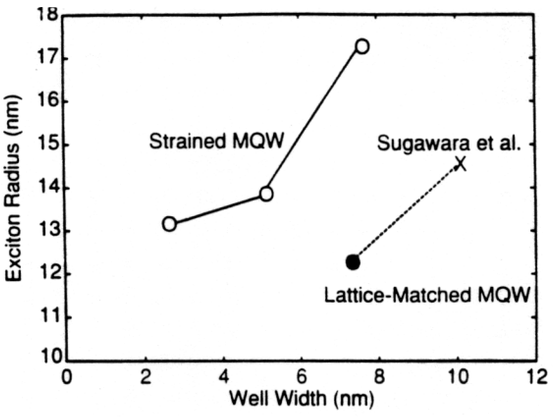

FIG. 8. Exciton radius as a function of well width for strained (open circle) and lattice-matched (closed circle) quantum wells. Cross is from Ref. 12. The lines are a guide to the eye.

linewidth due to structural fluctuations in the quantum well. It is also important in calculating the light intensity at which excitons start overlapping with each other and causing very strong optical nonlinearities. The integrated intensity of the exciton spectrum based on the effective-mass approximation is given by[12]

$$S=4e^2\hbar|(P_{CV})|^2|\langle\varphi_e(z)|\varphi_h(z)\rangle|^2/(\epsilon_0 cnm_0^2 E_{ph}\lambda_{ex}^2 L_z), \tag{20}$$

where e is the electron charge, P_{CV} is the optical matrix element, $\varphi_e(z)$ is the electron envelope wave function, $\varphi_h(z)$ is the hole envelope wave function, ϵ_0 is the permittivity in vacuum, c is the speed of the light, and n is the refractive index. The exciton radii were obtained using Eq. (20) by substituting experimental S values, which are 406, 240, 116, and 213 eV/cm for samples A–D, respectively. As shown in Fig. 8, the values are 13.1, 13.8, 17.2, and 12.2 nm for samples A–D, respectively. The increase of exciton radii is the main reason for small S values in the strained MQW structures.

C. Linewidth

The exciton spectrum broadening at low temperatures is primarily due to the spatial inhomogeneity of the exciton energy level caused by structural imperfections in the quantum wells,[50] such as interface roughness, composition fluctuations in constituent alloys, and nonperiodicity in multiple quantum wells. At high temperatures, the excitons are ionized to free electron-hole plasma by phonon scattering. The increase of phonons reduces the exciton lifetime, and broadens the excitonic transition spectrum according to the uncertainty principle. Figure 9 shows the room temperature FWHM (full width at half-maximum) of the heavy hole exciton peaks as a function of the well width. The data from Refs. 2, 11, 12, and 46 are also plotted. Reference 46 includes a FWHM value for a strained MQW. The dashed line is a guide to the eye. The values are in the range of 10–15 meV for both strained and lattice-matched MQW structures except at narrow well width. For the 2.5 nm well, the strained MQW structure

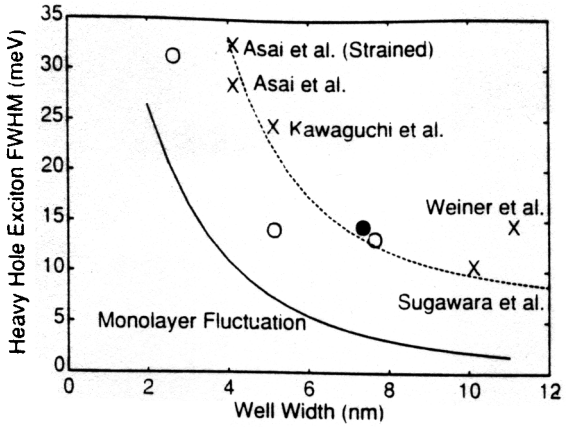

FIG. 9. Heavy hole exciton linewidth at room temperature as a function of well width for strained (open circle) and lattice-matched (closed circle) quantum wells. The data from Refs. 2, 11, 12, and 46 are also plotted (cross). The dashed line is a guide to the eye. The solid curve shows the calculated energy shift due to monolayer fluctuation.

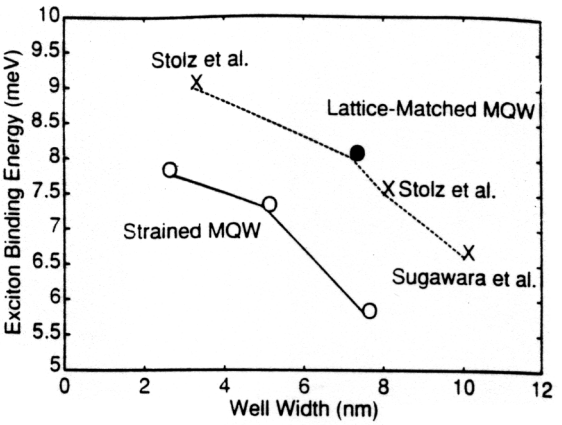

FIG. 10. Binding energy as a function of well width for strained (open circle) and lattice-matched (closed circle) quantum wells. The data from Refs. 8 and 12 are included (cross). The lines are a guide to the eye.

shows strong broadening as wide as 31 meV. To investigate this broadening, the theoretical subband energy change due to one monolayer fluctuation is also plotted in Fig. 9. It is reasonable to think that strong enhancement in the linewidth is partly due to the monolayer fluctuation of the quantum well which has comparable island size to the exciton radius. Statistical composition fluctuations may be another cause for this strong linewidth broadening.

The data in this study show narrower FWHM values than those of reported values.[11,46] The smaller number of quantum wells in our MQWs is thought to be one of the reasons. To reveal linewidth broadening mechanisms, low temperature measurements are also needed and are now under study. The PMT spectrum widths are also useful in studying $e1$-hh1 exciton linewidth. The broadening for 2.5 nm well is also observed in the PMT spectrum.

D. Binding energy and reduced effective mass

The two-dimensional exciton radius can be determined by a variational method by minimizing the exciton binding energy,[51,52]

$$E_b(\lambda_{ex}) = -\hbar^2/(2\mu\lambda_{ex}^2) + e^2\langle\Phi|1/\rho|\Phi\rangle/(4\pi\epsilon), \qquad (21)$$

where μ is the reduced effective mass parallel to the quantum well layers ($1/\mu = 1/m_{e\parallel} + 1/m_{hh\parallel}$) and $\rho = [r^2 + (z_e - z_h)^2]^{1/2}$, where z_e and z_h are the coordinates perpendicular to the plane of the layer of the electron and hole, respectively. The r is the relative position of electron and hole in the plane of the layer. The first term in the right-hand side in Eq. (21) is the kinetic energy of relative electron-hole motion in the quantum well plane. The second term is the Coulomb potential energy of the electron-hole relative motion. We know that a simple trial wave function of the ground state is

$$\Phi = \varphi_e(z_e)\varphi_h(z_h)\varphi_{ex}(r) \qquad (22)$$

with

$$\varphi_{ex}(r) = (2/\pi)^{1/2}\exp(-r/\lambda_{ex})/\lambda_{ex}, \qquad (23)$$

where λ_{ex} is the effective Bohr radius of the quasi bidimensional exciton. As we know the values of the exciton radii experimentally, the reduced effective mass and the binding energy can be calculated based on Eq. (21). The effective well widths were used for the calculation. Figure 10 shows the exciton binding energy as a function of the well width. Figure 10 includes the data for lattice-matched MQWs from Ref. 8, in which the values are determined by magnetoabsorption measurements and from Ref. 12. The E_b increases with decreasing well width and a value of 7.8 meV is obtained for a 2.5 nm strained layer MQW. The E_b seems to saturate in the narrow well width region for both lattice-matched and strained layer MQWs. The E_b is smaller for the strained MQWs than those for the lattice-matched MQWs by 1–2 meV.

Figure 11 shows the reduced effective mass as a function of the well width. Data for lattice-matched MQWs taken from Refs. 9 and 12 are also plotted. In Ref. 9, the values are determined by magnetoabsorption measurements. Small reduced effective masses for the strained layer MQWs are obtained. The values are in the range of 0.031–

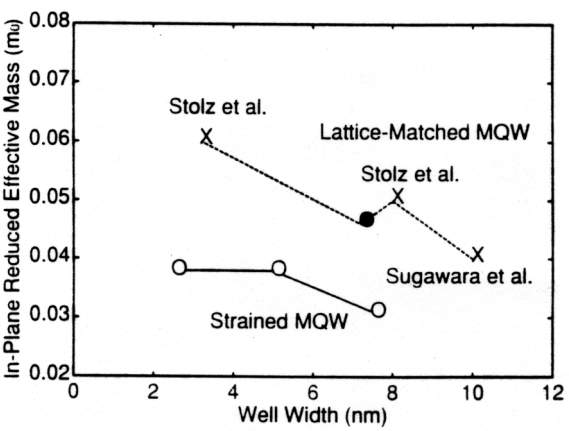

FIG. 11. In-plane reduced effective mass as a function of well width for strained (open circle) and lattice-matched (closed circle) quantum wells. The data from Refs. 9 and 12 are included (cross). The lines are a guide to the eye.

$0.038m_0$, which are 65% of those of the lattice-matched MQWs. It is well known that the heavy hole mass in the quantum well plane decreases with compressive strain. Our results reflect this strain effect as well as both the electron and hole effective mass changes due to a composition change in the well material. The calculations were carried t using simple models.[53,54] For well widths of 2.5–7.5 nm, the calculated reduced effective masses are 0.027–$0.032m_0$ for the strained structures, compared to 0.031–$0.039m_0$ for the lattice-matched structures. In spite of using simple models, the calculation results explain the decrease of the reduced effective masses qualitatively. This reduction of the reduced effective mass is the main reason for the large exciton radius and therefore the small integrated intensity for the strained layer MQW structures. In a sense, these results are negative for the application of the compressively strained MQWs in advanced devices which use excitonic effects such as quantum confined Stark effect[5] and optical Stark effect,[55,56] however, tensile strain may enhance the excitonic effect. The use of InGaAlAs for the well material is also promising, because the electron mass will be increased by the addition of Al. Femtosecond dynamics of excitons of these strained samples are also interesting properties, and will be studied.

IV. CONCLUSIONS

The physical properties of the room temperature excitons (transition energy, oscillator strength, linewidth, binding energy and reduced effective mass) in the compressively strained InGaAs/InGaAlAs multiquantum-well as a function of the well width were investigated by both absorption measurements and photomodulated transmittance (PMT) measurements. The PMT technique for the samples with a *p-i-n* structure is found to be very effective for revealing subband structures. Measured transition energies are in good agreement with the calculation which includes the heavy hole and light hole splitting due to strain. The oscillator strength for the same well width is smaller for the strained layer MQWs than those for the lattice-matched MQWs. This is due to the larger exciton radius for the strained layer MQWs resulting from the smaller in-plane reduced effective mass. The employment of tensile strain and the addition of Al to InGaAs well are proposed to increase the excitonic transition intensity. This new information is very important for application of strained layer MQWs to advanced photonic devices which use excitonic effects in MQW such as quantum confined Stark effect and optical Stark effect.

ACKNOWLEDGMENTS

One of the authors (Y.H.) would like to thank Professor E. P. Ippen for his continuous encouragement and useful discussions. This research was supported in part by the National Science Foundation, Contract No. ECS-9008485, and by the Army Research Office, Contract No. DAAL03-91-G-0051.

[1] D. S. Chemla, D. A. B. Miller, P. S. Smith, A. C. Gossard, and W. Wiegmann, IEEE J. Quantum Electron. **QE-20**, 265 (1984).
[2] J. S. Weiner, D. S. Chemla, D. A. B. Miller, T. H. Wood, D. Sivco, and A. Y. Cho, Appl. Phys. Lett. **46**, 619 (1985).
[3] D. A. B. Miller, D. D. Chemla, T. C. Damen, A. C. Gossard, W. Wiegmann, T. H. Wood, and C. A. Burrus, Phys. Rev. B **32**, 1043 (1985).
[4] K. Wakita, Y. Kawamura, Y. Yoshikuni, H. Asahi, and S. Uehara, IEEE J. Quantum Electron. **QE-22**, 1831 (1986).
[5] D. A. B. Miller, J. S. Weiner, and D. S. Chemla, IEEE J. Quantum Electron. **QE-22**, 1816 (1986).
[6] H. Temkin, M. B. Panish, and S. N. G. Chu, Appl. Phys. Lett. **49**, 859 (1986).
[7] M. Razeghi, J. Nagle, P. Maurel, F. Omnes, and J. P. Pocholle, Appl. Phys. Lett. **49**, 1110 (1986).
[8] W. Stolz, J. C. Maan, M. Altarelli, L. Tapfer, and K. Ploog, Phys. Rev. B **36**, 4301 (1987).
[9] W. Stolz, J. C. Maan, M. Altarelli, L. Tapfer, and K. Ploog, Phys. Rev. B **36**, 4310 (1987).
[10] D. J. Westland, A. M. Fox, A. C. Maciel, J. F. Ryan, M. D. Scott, J. I. Davies, and J. R. Riffat, Appl. Phys. Lett. **50**, 839 (1987).
[11] Y. Kawaguchi and H. Asahi, Appl. Phys. Lett. **50**, 1243 (1987).
[12] M. Sugawara, T. Fujii, S. Yamazaki, and K. Nakajima, Phys. Rev. B **42**, 9587 (1990).
[13] D. Gershoni, H. Temkin, M. B. Panish, and R. A. Hamm, Phys. Rev. B **39**, 5531 (1989).
[14] N. Yokouchi, T. Uchida, T. Uchida, T. Miyamoto, F. Koyama, and K. Iga, Jpn. J. Appl. Phys. **30**, L885 (1991).
[15] T. Y. Wang and G. B. Stringfellow, J. Appl. Phys. **67**, 344 (1990).
[16] A. R. Adams, Electron. Lett. **22**, 249 (1986).
[17] E. Yablonovitch and E. O. Kane, IEEE J. Lightwave Technol. **LT-4**, 504, 961E (1986).
[18] E. Yablonovitch and E. O. Kane, IEEE J. Lightwave Technol. **LT-6**, 1292 (1988).
[19] I. Suemune, L. A. Coldren, M. Yamanishi, and Y. Kan, Appl. Phys. Lett. **53**, 1378 (1988).
[20] P. J. A. Thijs, L. F. Tiemeijer, P. I. Kuindersma, J. J. M. Binsma, and T. V. Dongen, IEEE J. Quantum Electron. **QE-27**, 1426 (1991).
[21] J. S. Osinski, P. Grodzinski, Y. Zou, and P. D. Dapkus, Electron. Lett. **27**, 469 (1991).
[22] U. Koren, M. Oron, M. G. Young, B. I. Miller, J. L. De Miguel, G. Raybon, and M. Chien, Electron. Lett. **26**, 465 (1990).
[23] H. Yamada, M. Kitamura, and I. Mito, presented at the Device Research Conference, 1990 (unpublished), Paper IVB-2.
[24] T. Tanbun-Ek, R. A. Logan, N. A. Olsson, H. Temkin, A. M. Sergent, and K. W. Wecht, in Technical Digest of the 12th IEEE International Semiconductor Laser Conference, Davos, 1990 (unpublished), p. 46.
[25] M. Okamoto, K. Sato, H. Mawatari, F. Kano, K. Magari, Y. Kondo, and Y. Itaya, IEEE J. Quantum Electron. **QE-27**, 1463 (1991).
[26] M. C. Tatham, C. P. Seltzer, S. D. Perrin, and D. M. Cooper, Electron. Lett. **27**, 1278 (1991).
[27] C. E. Zah, R. Bhat, B. Pathak, C. Caneau, F. J. Favire, N. C. Andreadakis, D. M. Hwang, M. A. Koza, C. Y. Chen, and T. P. Lee, Electron. Lett. **27**, 1414 (1991).
[28] C. E. Zah, R. Bhat, F. J. Favire, Jr., S. G. Menocal, N. C. Andreadakis, K. W. Cheung, D. M. D. Hwang, M. A. Koza, and T. P. Lee, IEEE J. Quantum Electron. **QE-27**, 1440 (1991).
[29] N. K. Dutta, H. Temkin, T. Tanbun-Ek, and R. Logan, Appl. Phys. Lett. **57**, 1390 (1990).
[30] Y. Hirayama, M. Morinaga, M. Tanimura, M. Onomura, M. Funemizu, M. Kushibe, N. Suzuki, and M. Nakamura, Electron. Lett. **27**, 241 (1991).
[31] Y. Hirayama, M. Morinaga, N. Suzuki, and M. Nakamura, Electron. Lett. **27**, 875 (1991).
[32] Y. Hirayama, M. Morinaga, M. Onomura, M. Tanimura, M. Tohyama, M. Funemizu, M. Kushibe, N. Suzuki, and M. Nakamura, IEEE J. Lightwave Technol. **LT-10**, 1272 (1992).
[33] H. Yasaka, R. Iga, Y. Noguchi, and Y. Yoshikuni, IEEE Photon. Technol. Lett. **PTL-4**, 826 (1992).
[34] J. D. Evans, T. Makino, N. Puetz, J. G. Simmons, and D. A. Thompson, IEEE Photon. Technol. Lett. **PTL-4**, 299 (1992).
[35] W.-Y. Choi and C. G. Fonstad, J. Cryst. Growth **127**, 559 (1993).
[36] J. W. Matthews and A. E. Blakeslee, J. Cryst. Growth **27**, 118 (1974).

[37] M. Gendry, V. Drouot, C. Santinelli, and G. Hollinger, Appl. Phys. Lett. **60**, 2249 (1992).
[38] A. Frova, P. Handler, F. A. Germano, and D. E. Aspnes, Phys. Rev. **145**, 575 (1966).
[39] C. V. Hoof, D. J. Arent, K. Deneffe, J. De Boeck, and G. Borghs, J. Appl. Phys. **64**, 4233 (1988).
[40] J. L. Shay, Phys. Rev. B **2**, 803 (1970).
[41] B. V. Shanabrook, O. J. Glembocki, and W. T. Beard, Phys. Rev. B **35**, 2540 (1987).
[42] W. M. Theis, G. D. Sanders, C. E. Leak, K. K. Bajaj, and H. Morkoç, Phys. Rev. B **37**, 3042 (1988).
[43] C. G. Van de Walle, Phys. Rev. B **39**, 1871 (1989).
[44] C. G. Van de Walle, Phys. Rev. B **35**, 8154 (1987).
[45] D. Olego, T. Y. Chang, E. Silberg, E. A. Caridi, and A. Pinczuk, Appl. Phys. Lett. **41**, 476 (1982).
[46] H. Asai and Y. Kawamura, Appl. Phys. Lett. **56**, 746 (1990).
[47] J. I. Davies, A. C. Marshall, M. D. Scott, and R. J. M. Griffiths, Appl. Phys. Lett. **53**, 276 (1988).
[48] W. T. Masselink, P. J. Pearah, J. Klem, C. K. Peng, H. Morkoç, G. D. Sanders, and Y.-C. Chang, Phys. Rev. B **32**, 8027 (1985).
[49] J. M. Rorison and D. C. Herbert, Superlatt. Microstruct. **1**, 423 (1985).
[50] S. Hong and J. Singh, J. Appl. Phys. **62**, 1994 (1987).
[51] G. Bastard, E. E. Mendez, L. L. Chang, and L. Esaki, Phys. Rev. B **26**, 1974 (1982).
[52] G. Bastard, E. E. Mendez, L. L. Chang, and L. Esaki, Phys. Rev. B **28**, 3241 (1983).
[53] U. Ekenberg, Phys. Rev. B **40**, 7714 (1989).
[54] B. K. Ridley, J. Appl. Phys. **68**, 4667 (1990).
[55] A. Von Lehmen, D. S. Chemla, J. E. Zucker, and J. P. Heritage, Optics Lett. **11**, 609 (1986).
[56] A. Mysyrowicz, D. Hulin, A. Antonetti, A. Migus, W. T. Masselink, and H. Morkoç, Phys. Rev. Lett. **56**, 2748 (1986).